npj | climate and atmospheric science

www.nature.com/npjclimatsci

ARTICLE OPEN

Check for updates

Subseasonal controls of U.S. landfalling tropical cyclones

Baoqiang Xiang[1,2✉], Bin Wang[3], Wei Zhang[4], Lucas Harris[1], Thomas L. Delworth[1], Gan Zhang[1,5,6] and William F. Cooke[1]

Landfalling tropical cyclones (LTCs) are the most devastating disaster to affect the U.S., while the demonstration of skillful subseasonal (between 10 days and one season) prediction of LTCs is less promising. Understanding the mechanisms governing the subseasonal variation of TC activity is fundamental to improving its forecast, which is of critical interest to decision-makers and the insurance industry. This work reveals three localized atmospheric circulation modes with significant 10–30 days subseasonal variations: Piedmont Oscillation (PO), Great America Dipole (GAD), and the Subtropical High ridge (SHR) modes. These modes strongly modulate precipitation, TC genesis, intensity, track, and landfall near the U.S. coast. Compared to their strong negative phases, the U.S. East Coast has 19 times more LTCs during the strong positive phases of PO, and the Gulf Coast experiences 4–12 times more frequent LTCs during the positive phases of GAD and SHR. Results from the GFDL SPEAR model show a skillful prediction of 13, 9, and 22 days for these three modes, respectively. Our findings are expected to benefit the prediction of LTCs on weather timescale and also suggest opportunities exist for subseasonal predictions of LTCs and their associated heavy rainfalls.

npj Climate and Atmospheric Science (2022)5:66 ; https://doi.org/10.1038/s41612-022-00289-9

INTRODUCTION

Landfalling tropical cyclones (LTCs) formed in the North Atlantic induce a significant toll on human life and property. Coastal regions are most vulnerable to TC-induced damages, while many inland regions sometimes suffer through TC-related extreme rainfall and devastating floods. Compared to many other extreme weather and climate disasters, the losses from TCs dominate the distribution of damage for the U.S. For example, 15 out of the top 20 most costly billion-dollar-plus weather climate disasters in the U.S. are due to landfalling hurricanes from 1980 to 2020[1]. LTCs also have the highest average event cost for the U.S.[2,3].

Due to societal need, increasing the predictive capability of TCs is one of the top priorities in the weather and climate communities. A skillful TC prediction is critical for timely and effective preparedness. Early preparation leads to a substantial reduction of loss of life and property associated with these storms[4]. Along with the advances in dynamical forecast systems and computational resources, TC prediction has achieved substantial progress on both weather[5–7] and seasonal timescales in recent decades[8–10].

Subseasonal prediction (between 10 days and one season) has garnered great interest in recent decades as a focused effort to bridge the gap between the weather and seasonal forecasts. However, subseasonal prediction is still in its infancy and remains challenging. The majority of current dynamical models only show useful TC prediction in terms of genesis and tropical storm days (TSDs) (also called TC track density) within 1 week[11–15]. So far, there is little evidence in the literature of skillful subseasonal LTC prediction near the U.S. coast.

The potential in predicting LTCs takes root in understanding the dominant factors accounting for the variations in the genesis frequency and tracks of TCs. Some factors have been reported to be essential in regulating the U.S. LTCs on interannual to decadal timescales, such as the Atlantic and tropical sea surface temperature[16,17], El Niño/Southern Oscillation (ENSO)[2,18], Atlantic Multidecadal Oscillation (AMO)[19], the summertime North Atlantic Oscillation (NAO)[20–23], and the Pacific Meridional Mode (PMM)[24].

What controls the TC landfalls on the subseasonal timescale? The Madden–Julian Oscillation (MJO), a dominant 30–60-day oscillatory mode in the tropics[25,26], has been demonstrated to play an important role in modulating the TC activity in the Gulf of Mexico and the landfall probability in the Gulf Coast[27–31]. Although these previous studies would suggest the MJO as a crucial source of subseasonal TSD predictability, here, we find that the TSD power spectra over both the Gulf of Mexico and the eastern U.S. coast have more significant peaks on shorter timescales (10–30 days) than that of the MJO (Fig. 1). We, therefore, hypothesize that some previously unknown processes and mechanisms regulate the observed subseasonal variability of TCs. The goal of this research is to identify the major processes controlling the subseasonal TC activity near the U.S. coasts and then explore their predictive skills from a newly developed dynamical model.

RESULTS

Distinct modes of North American Subseasonal Variability (NASV)

The LTC frequency is tightly linked to both TC track and genesis. The TC track is primarily controlled by steering flow that can be approximately represented by the lower-tropospheric circulation near the U.S. coast, given the high correlation between the 850 hPa and 500 hPa geopotential height anomalies (Supplementary Fig. 1). The factors determining the subseasonal modulation of TC genesis by MJO and Boreal Summer Intraseasonal Oscillation (BSISO)[32,33] are to some extent different from the factors controlling the seasonal TC genesis[34–36] and are also basin-dependent[36]. The most prominent controlling factor is the 500 hPa vertical motion for most basins, except the western North Atlantic, where the relative vorticity in the lower-troposphere plays the dominant role in determining the

[1]NOAA/Geophysical Fluid Dynamics Laboratory, Princeton, NJ, USA. [2]University Corporation for Atmospheric Research, Boulder, CO, USA. [3]Department of Atmospheric Sciences and International Pacific Research Center, University of Hawaii, Hawaii, HI, USA. [4]Department of Plants, Soils and Climate, Utah State University, Logan, UT, USA. [5]Atmospheric and Oceanic Sciences Program, Princeton University, Princeton, NJ, USA. [6]Present address: Now at Citadel Americas LLC, Chicago, IL, USA. ✉email: baoqiang.xiang@noaa.gov

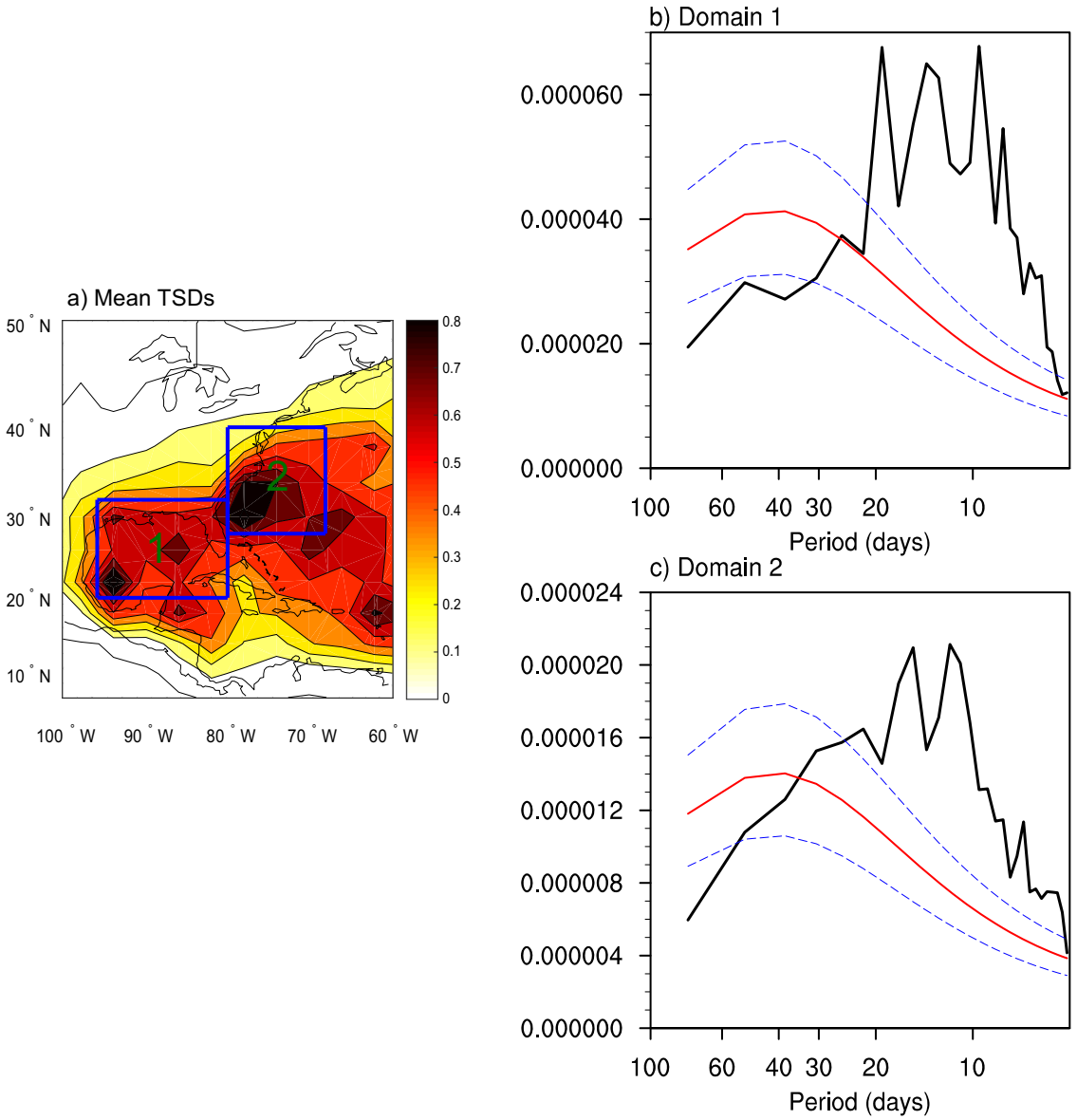

Fig. 1 Tropical storm days (TSDs) and their power spectra. a Climatological TSDs (per 100 days) during June–October, and the power spectra of 3-day running mean TSDs over the **b** domain 1 and **c** domain 2 shown in **a**.

subseasonal variability of TC genesis[36]. Motivated by this, we focus on understanding the major atmospheric circulation modes in the lower troposphere that may influence both TC track and genesis.

To highlight the subseasonal variation, an Empirical Orthogonal Function (EOF) analysis is performed using observed 3-day running mean 850 hPa geopotential height (H850) anomalies during the Atlantic TC season (June–October). The studied domain (100°W–70°W, 10°N–40°N) covers the majority of the regions that LTCs can potentially impact. This analysis yields three distinctive modes that explain about 49.4%, 17.6%, and 13.9% of the total H850 variance. The fourth mode explains a much smaller portion of the total variance (4.8%). The first EOF mode (EOF1) shows a predominance of an anomalous low pressure centered in the eastern U.S. (Fig. 2a). The second EOF mode (EOF2) resembles a zonal dipole pattern. A low anomaly is centered in the western U.S. with a trough extending southeastward to the Gulf of Mexico, and the high anomaly is centered in the east coast of the U.S. (Fig. 2b). The third EOF mode (EOF3) features a meridional dipole pattern with a low centered at the Caribbean Sea and a high over central-eastern North America (Fig. 2c). Note that these three leading modes are still present over a much larger domain (see Methods).

Investigation of their principle components (PCs) reveals significant peaks on the subseasonal timescale (10–30 day) relative to a red noise process in the spectra for all three modes (Fig. 2d–f). Note that these three modes are distinguished from the canonical MJO or BSISO mode with a spectral peak at 30–60 days (Supplementary Table 1). Compared to the EOF patterns derived from 3-day running mean data, similar patterns can be obtained using band-pass filtered (10–35 day) H850 anomalies (Fig. 2g–i), confirming the predominance and robustness of the subseasonal components. The simultaneous 500 hPa geopotential height anomalies display a rather localized feature residing in the eastern U.S. for the EOF1 mode (Fig. 2g). The EOF2 mode has a clear zonal wave train pattern (Fig. 2h), and EOF3 displays a meridional land-sea contrasting structure mainly representing a northeast migration of the North Atlantic Subtropical High (NASH) ridge[37] (Fig. 2i). For simplicity, hereinafter we refer to these three NASV modes as Piedmont Oscillation (PO), Great American Dipole (GAD), and subtropical high ridge (SHR)

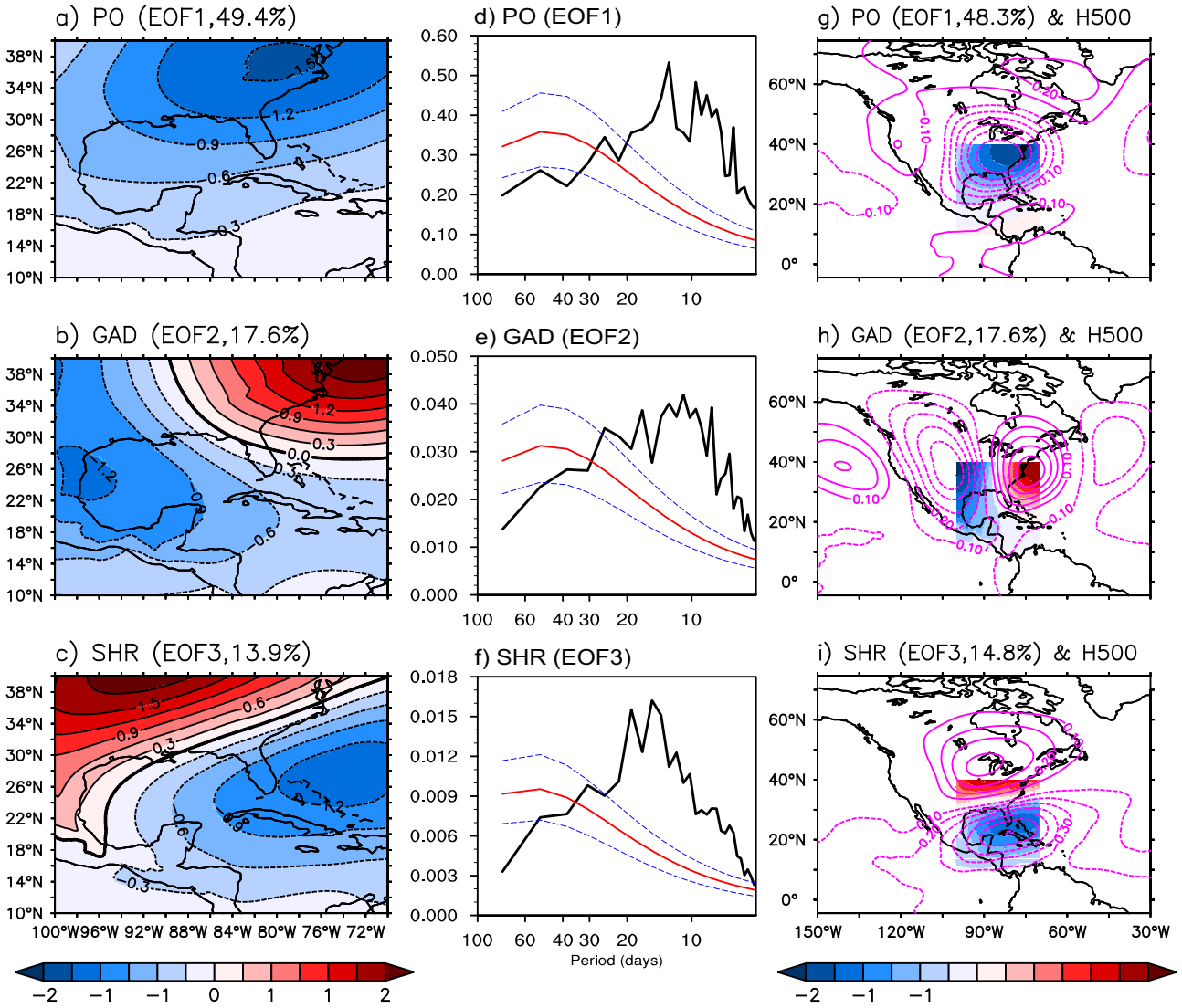

Fig. 2 The leading circulation modes and their power spectra. a–c the leading EOF modes of 3-day running mean 850 hPa geopotential height (H850) anomalies. **d–f** the power spectra of the first three modes shown in **a–c**, with the upper and lower blue dashed lines representing the 95% and 5% confidence limits for this red noise. Note that the spectra are calculated for individual hurricane seasons and is then averaged over multiple years. **g–i** the first three modes of band-pass filtered (10–35 days) H850 anomalies (shading, the EOF domain and colorscale are the same as **a–c**), and the simultaneous correlation between the PCs and the band-pass filtered (10–35 days) 500 hPa geopotential height anomalies (contours).

mode, respectively. Some simple indices can be constructed as a surrogate for these three modes and they are highly correlated with the PCs (see Methods).

The first two NASV modes' centers reside to the south of the Atlantic midlatitude jet, and their formation and evolution are likely linked to the transient eddies that develop in the midlatitude baroclinic zones. For example, the PO and GA modes are accompanied by prominent variations of Rossby wave breaking (RWB) (see Methods) near the U.S. East Coast (Supplementary Fig. 2), which vary together with Rossby wave trains across North America[38]. These extratropical perturbations can affect environmental variables in TC-prone regions and have been suggested to modulate the subseasonal variations and predictability of Atlantic TCs[14]. The SHR mode is likely linked to the NASH center's variation[37].

These three modes are also robust on synoptic timescales, together with a similar but relatively weak regulation effect on the coastal TC activity (Supplementary Fig. 3). This indicates that the formation and maintenance of these modes are intrinsically linked to the land-ocean configuration in the studied domain, while the underlying physical mechanism warrants further study.

Impacts of the NASV modes on the TC activity near the U.S. coast

To identify the potential impacts of these NASV modes on TCs (defined as storms with a lifetime maximum sustained surface wind speed ≥17.5 m/s), we perform a composite analysis of TC activity during the strong positive (normalized Principal Component (PC) > 1) and negative (normalized PC < −1) phases of these three modes (Fig. 3). Note that the PCs are based on the EOF analysis of the band-pass filtered (10–35 days) H850 anomalies. We first examine the impacts of these modes on TC genesis (the TC genesis location is defined as the first position where the maximum sustained wind speed exceeds 17.5 m/s). For SHR, more TC geneses occur during their positive phases, particularly over the Gulf of Mexico (Fig. 3), increasing the chances of landfalls in the following days. In contrast, for PO, there is less TC genesis

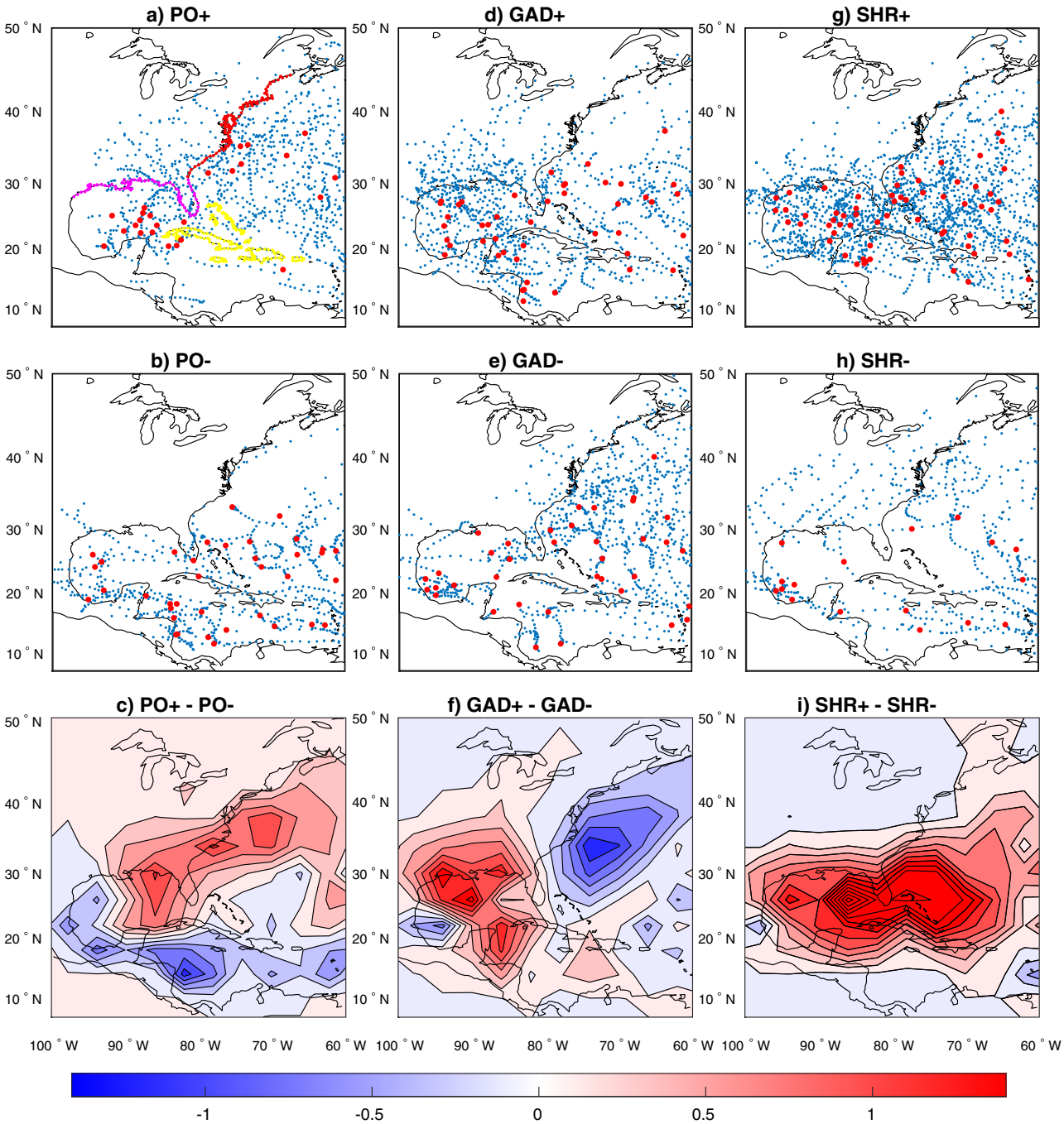

Fig. 3 Modulation of tropical cyclone (TC) activity by three subseasonal modes. a, **b** the TC positions (every 6 h) including their geneses (red dots) during the strong positive (normalized PC > 1) and negative (normalized PC < −1) phases of EOF1 modes derived from the band-pass filtered (10–35 days) H850 anomalies. **c** the TSDs (per 100 days) difference between the strong positive and negative phases of EOF modes. The right two columns are similar to the left column but for EOF2 (**d**–**f**) and EOF3 (**g**–**i**) modes, respectively. The magenta, red, and yellow coastal lines in a) represent the individual landfalling regions: Gulf Coast, East Coast, and the Caribbean, respectively.

during its positive phases than its negative phase, together with a latitudinal contrast in terms of genesis locations (Fig. 3a vs. b). One common feature is that more TC geneses are observed in the Gulf of Mexico during their positive phases for all three modes.

TC track is also substantially influenced by these NASV modes. During the positive phases of PO when the low pressure is centered in the eastern U.S., enhanced TC activity is observed in the majority of the U.S. coastal regions although it has the tendency to push TC away from the coast over the regions north of ~35°N (Fig. 3a). During its negative phases, the TC activity is largely suppressed near the U.S. coasts (Fig. 3b). The corresponding difference of tropical storm days (TSDs) between these two phases evidently illustrates more LTCs during the positive phases than the negative phases (Fig. 3c). During the strong positive phases of GAD when the low-pressure dominates the western U.S. and Gulf of Mexico, active TCs are observed in the Gulf of Mexico but very few TCs appear to the east of the U.S. coast (Fig. 3d). It has an opposite TC modulation effect during the negative phases (Fig. 3e). The TSDs difference between these two phases reveals a consistent dipole pattern between the Gulf of Mexico and the

Table 1. TC Landfall rate (per 100 days) during the strong positive (PC > 1), neutral (|PC| < 0.5), and strong negative (PC < −1) phases of three EOF modes in three regions as shown in Fig. 3a.

	Gulf coast	East coast	Caribbean
EOF1+	2.11	2.32*	1.28
EOF1 neutral	1.55	1.15	1.52
EOF1−	0.80*	0.12*	1.28
EOF2+	3.74*	0.68*	1.64
EOF2 neutral	1.71	1.08	1.68
EOF2−	0.86*	1.10	1.02*
EOF3+	4.83*	1.05	4.03*
EOF3 neutral	1.36	1.50	1.20
EOF3−	0.40*	0.59*	0.73*

The values with * represent they are statistically significantly different from their neutral phases at the 5% level.
Note that the EOF analysis is based on band-pass filtered (10–35 days) H850 anomalies.

region to the east of the U.S. coast (Fig. 3f). During the strong positive phases of the SHR mode, the large-scale low-pressure system tends to favor TC genesis in the Gulf of Mexico, the north Caribbean Sea, and the regions to the east of Florida (Fig. 3g), and vice versa for the negative phases (Fig. 3h). Note that the modulation of TCs by the SHR mode exhibits a similar pattern with an MJO mode originating from the eastern Pacific[29], but they differ in timescales.

These three NASV modes strikingly modulate the LTCs frequency along the U.S. coast. Here we define three regions: Gulf Coast, the East Coast, and the Caribbean (Fig. 3a and Table 1). Compared to the neutral phases of PO (|PC| < 0.5), there are ~202% (10%) of landfalls (see Methods) in the East Coast during the strong positive (negative) phases of PO. For GAD, the strong positive (negative) phases show around 219% (50%) of landfalls in the Gulf Coast. During the strong positive (negative) phases of the SHR mode, the TCs are 355% (29%) as likely to make landfall in the Gulf Coast, and 336% (61%) in the Caribbean regions compared to their neutral phases. The contrast is even more pronounced by comparing the strong positive and negative phases. For example, the U.S. East Coast experiences 19 times more LTCs during the strong positive phases of PO, and the Gulf Coast has about 4–12 times more chances to have LTCs during the positive phases of GAD and SHR with the reference of their corresponding negative phases (Table 1). In short, the PO mode exerts pronounced impacts on the TC landfalls near the U.S. East Coast, while the circulation related to the GAD and the SHR modes plays a critical role in governing the TC landfalls near the Gulf Coast. These modes also strongly affect the TC intensity near the coastal regions: more intense TCs are observed to the east of the U.S. (Gulf of Mexico) for the PO (GAD) mode during its strong positive phases, while the TC intensity tends to be stronger over both regions during the strong positive phases of the SHR mode (Supplementary Fig. 4).

The rainfall anomalies differ dramatically among these three modes, as revealed by the composite differences between their strong positive and negative phases (Fig. 4). For PO, enhanced precipitation covers the majority of the eastern U.S. coastal regions, with its maximum centered in the surrounding oceans (Fig. 4a). For GAD, conspicuously increased rainfall is located in the majority of the Gulf of Mexico, the central-to-eastern U.S., with its maximum confined to the central Gulf states, including TX, LA, MS, AL, and AR (Fig. 4b). A region of concurrent suppressed precipitation occurs in the northwestern Atlantic. The strong positive phases of the SHR mode lead to excessive rainfall to the east of the Gulf of Mexico and the Caribbean regions, accompanied by a modest precipitation deficit in the central-to-eastern continental U.S. (Fig. 4c). Note that the impacts between the positive and negative phases largely mirror each other for these three modes (not shown). Both large-scale circulations and TCs contribute to the observed rainfall anomalies. For GAD, the strong rainfall anomalies over the inland states are mainly due to large-scale circulations through strengthening the Great Plains Low-Level Jet[39] (Fig. 4). Over the ocean and coastal regions, TC-induced rainfall anomalies can explain about 20–50% of the total rainfall anomalies. However, it accounts for most of the heavy rainfall events (Methods, and Fig. 4d–f).

How do these NASV modes affect the U.S. coastal TC activity? First, they largely alter the steering flows as well as TC landfall probability. The positive phases of PO concur with strong southwesterly wind anomalies along the southern and eastern U.S. coasts (Fig. 4a, c), favoring TC landfalls. For GAD, anomalous southerly winds near the Gulf of Mexico (Fig. 4b) lead to northward TC tracks together with active TC landfalls in the surrounding regions. Second, these modes also modulate the environments relevant to TC genesis. For instance, the positive phases of PO (SHR) are accompanied by an anticyclonic (cyclonic) circulation over the surrounding oceans (Fig. 2). The resultant changes of lower-tropospheric relative vorticity explain, at least partially, their contrasting TC genesis frequency as well as the subsequent landfalling TC rate. The 500 hPa vertical motion may also play some role in affecting TC genesis while the associated vertical wind shear seems less important (Supplementary Fig. 5).

The links between TC activity and these modes display salient seasonal dependence. More remarkable TC modulations are present in boreal summer than boreal autumn for GAD, while it tends to be opposite for the PO and the SHR modes (Supplementary Fig. 6). This is related to both the seasonal migration of TC activity and the seasonal change in the variance of these three modes (Supplementary Fig. 7).

Model reproducibility and predictability of the NASV modes

How well do the current dynamical forecast models simulate these modes? Whether and to what extent can these modes be predicted? Here we use a recently developed Geophysical Fluid Dynamics Laboratory (GFDL) Seamless System for Prediction and Earth System Research (SPEAR) model to address these questions[40]. From a 50-yr control simulation, the model well captures these three modes, with similar spatial patterns, power spectra (Supplementary Fig. 8), and also TC modulation impacts (Supplementary Fig. 9) to those of observations. The successful simulation of these modes in the control simulation provides a precondition for a skillful prediction of these modes.

Based on 20-yr (2000–2019) hindcast results using the SPEAR model[41], we evaluate both the anomalous correlation coefficient (ACC) and mean square skill score (MSSS) (see Methods) of these three NASV modes for the cases initialized during June–October (Fig. 5). Note that the forecasted PCs are obtained by projecting the forecast data anomalies onto the observed EOF patterns (Fig. 2g–i). This analysis reveals that these three modes (PO, GAD, SHR) can be skillfully predicted with a lead time of 13, 9, and 22 days, respectively, as determined by the time when the MSSS drops to 0. These skills are roughly corresponding to the time when the ACC drops to 0.4. This is generally outside the predictability horizons of canonical weather forecasting, so these three modes potentially have profound importance for predicting the TC activity on both weather and subseasonal timescales. It also provides different upper limits (potential predictability) of the deterministic TC prediction influenced by these three modes in this model: the GAD-related TCs are less predictable than those associated with PO and SHR. The difference in their prediction skill is related to the geographical distribution of their major loadings

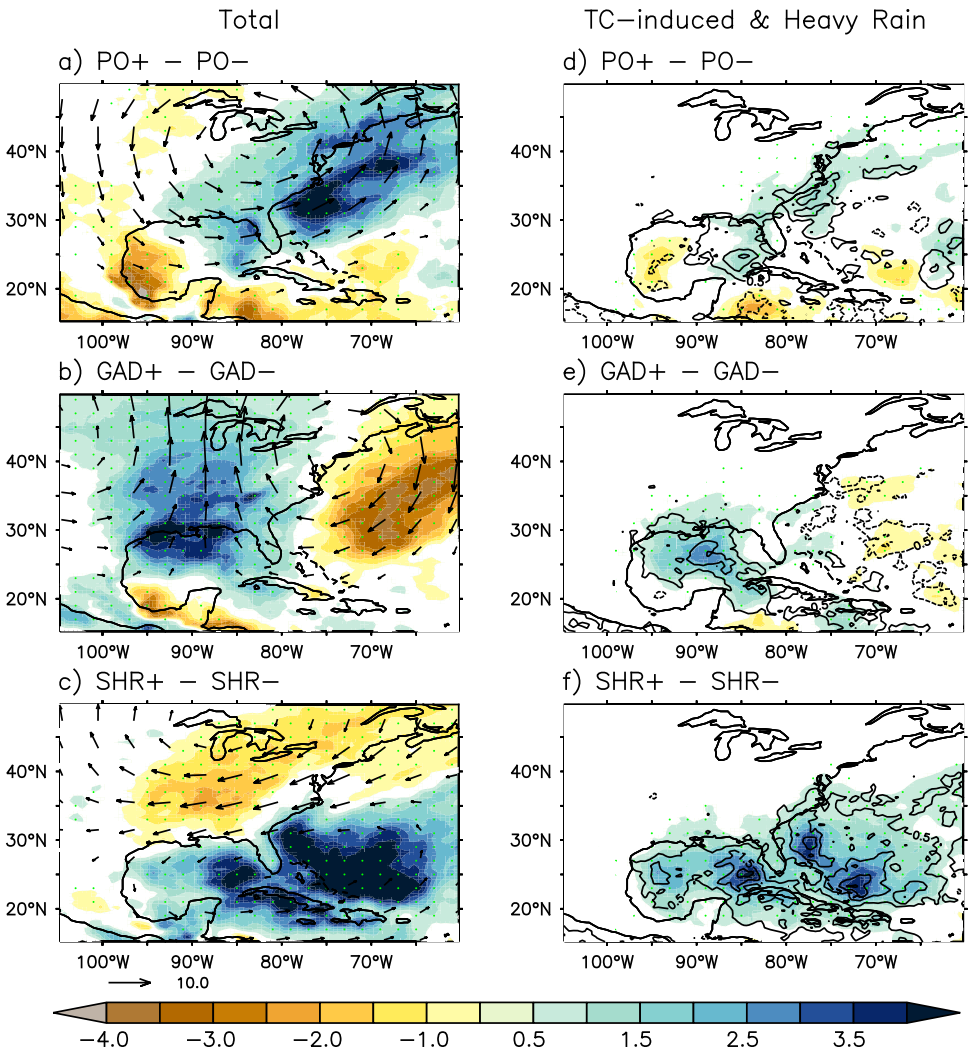

Fig. 4 Precipitation changes related to the leading three subseasonal circulation modes. a–c the composite difference of band-pass filtered (10–35 day) precipitation (shading in mm per day) and 500 hPa winds (vectors, not shown when the speed anomalies are <1.5 m s^{-1}) between the strong positive (PC > 1) and negative (PC < −1) phases of these three modes. **d–f** Similar to the **a–c** but for TC-induced precipitation only (shading) and the heavy precipitation anomalies (contours with interval of 1 mm per day). The green stippling denotes the regions with composites that are significant at the 5% level for precipitation anomalies (left panel) and the TC-induced precipitation (right panel).

(generally higher prediction skill for the mode in lower latitudes than that in higher latitudes, and higher skill over the ocean than over the land).

DISCUSSION

We have identified three major subseasnonal modes (Fig. 6) that show strong modulation on the TC activities near the U.S. coast. What is the nature of these NASV modes? Are these modes locally or remotely forced? To answer this, we examine the lead-lag relationship between these modes and 500 hPa geopotential height anomalies (Fig. 2g–i, Supplementary Fig. 10) as well as precipitation anomalies (Supplementary Fig. 11). With the absence of tropical signals, the PO and SHR modes appear to be quasi-stationary, and GAD has a weak eastward propagation tendency. This implies that all these modes are locally excited and maintained, largely independent from other modes, such as MJO, BSISO, North Atlantic Oscillation (NAO), and Pacific-North American (PNA) pattern (Supplementary Table 1).

Improved TC prediction near the U.S. coast is not only of vital importance from a scientific standpoint but also has profound socio-economic repercussions. The present findings provide dynamical insights about the mechanisms determining the subseasonal TC activity near the U.S. coast, differing substantially from that for the interannual to decadal variations[2,16–24]. The beyond-weather timescale prediction of these modes will benefit the TC (genesis, track, and landfall) prediction on weather timescale and also suggests opportunities exist for subseasonal predictions of TCs and their associated heavy rainfalls. Considering the relatively simple initialization largely limiting its capability in predicting TCs (especially tracks) in the current dynamical model, a thorough investigation of the prediction of LTCs associated with these NASV modes is planned using the GFDL SHiELD model with a higher-resolution and more sophisticated initialization[42]. How do these modes change along with global warming is another interesting topic calling for deliberation.

METHODS

Data

In this study, several datasets are used including the daily mean geopotential height from ERA-5 reanalysis data as observations (C3S,

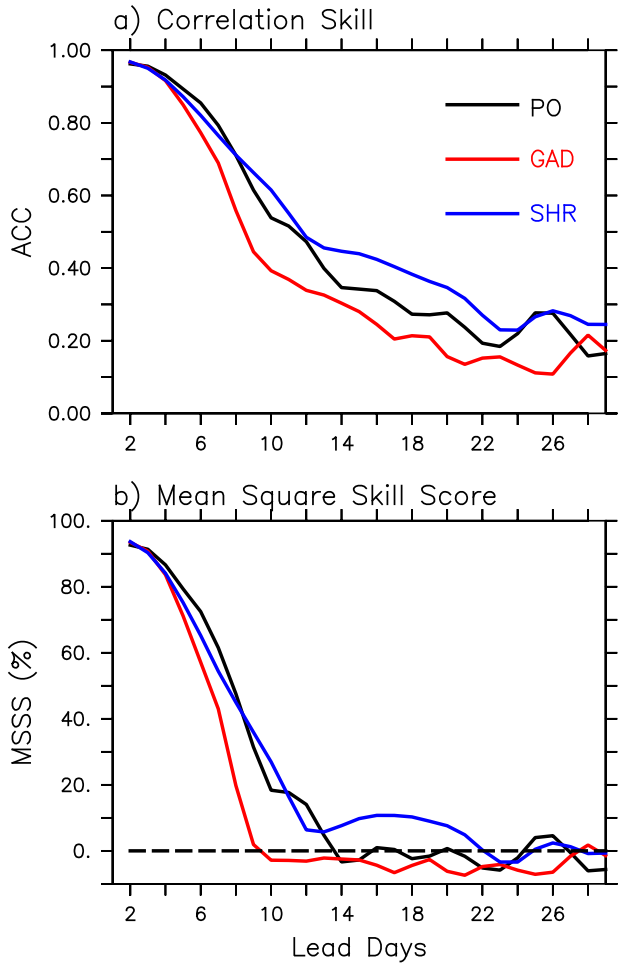

Fig. 5 Prediction of the PCs of leading three subseasonal circulation modes in the GFDL SPEAR model. a The anomalous correlation skill of PCs for these three modes as a function of the lead time. **b** is similar to **a** but for the mean square skill score (MSSS) of PCs for these three modes.

2017), the NOAA daily mean interpolated OLR data[43], and precipitation from Multi-Source Weighted-Ensemble Precipitation (MSWEP)[44]. The observational anomalies were obtained by removing the time mean and the first three harmonics of the observational climatological annual cycle. The observational TC data is obtained from the National Hurricane Center[45]. We select the storms with at least one label of "HU" (hurricane) or "TS" (tropical storm) and a lifespan of at least 1 day in the database. Note that extratropical storms are included here. The studied period covers the time range from 1979 to 2018, except the MSWEP precipitation data that is available from 1979 to 2016.

Robustness of the NASV modes

To test whether the identified NASV modes are robust or not, we conduct a lot of tests and the results are generally robust. Here is one example. If we choose a larger domain (130W-50W,5S-45N, about 4.4 times larger than the original domain) and these three modes are still robust although the fourth and third modes change their order (Supplementary Fig. 12). But if we further expand the domain, for example, the North America and north Atlantic (130°W–0°, 5°S–65°N), the first three modes are very different, but these modes have no evident impacts on the TC activity near the US coast.

To understand whether these modes are due to the variations of TCs, we also investigate the TC-related H850 anomalies by considering the grid points within 500 km of the storm center. Results show that the TC-related H850 anomalies are much smaller than the total H850 anomalies, confirming that the formation of these NASV modes is not due to TCs.

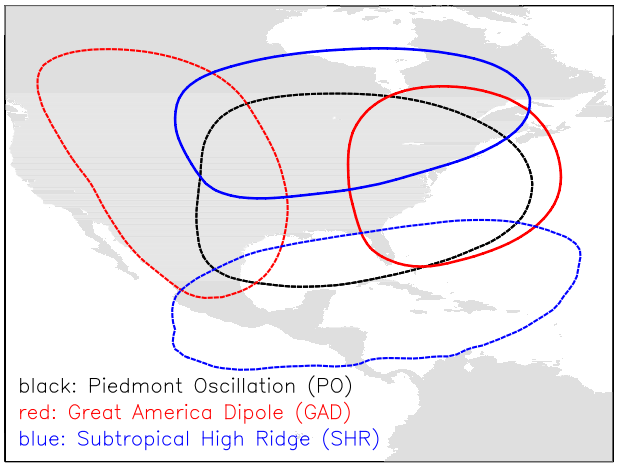

Fig. 6 A sketch diagram showing the main action centers of these three NASV modes. Solid lines represent high-pressure centers and the dashed lines denote low-pressure centers.

Reconstructed indices representing these three EOF modes

To represent these three subseasonal EOF modes, we build indices based on H850 anomalies normalized by their observed local variance using the band-pass filtered (10–35 days) data:

For PO: H850(95W-70W, 25N-40N)/119.0*(-1)

For GAD: H850(77W-65W, 30N-40N)/168.5- H850(105W-90W, 15N-40N)/89.2

For SHR: H850(100W-70W, 38N-45N)/177.2- H850(90W-70W, 15N-30N)/69.1

These reconstructed indices are highly correlated with the PCs of these modes ($r = 0.99$, 0.97, 0.95, respectively).

Detection of Rossby wave breaking (RWB)

RWB is identified based on potential vorticity (PV) overturning on the 350-K isentropic surface following previous studies[46,47]. The 350-K isentropic surface approximately corresponds to the upper troposphere and/or the lower stratosphere, where Rossby wave activity is relatively strong. The RWB search algorithm finds the meridional overturning features on PV contours at 0.5-PVU intervals (1 PVU = 10–6 K kg^{-1} m^2 s^{-1}). Features in each other's vicinity at the same time step are assumed to be related to the same breaking wave, so the algorithm only retains the feature with the largest spatial extent. Similar to Zhang, et al.[48], we count the centroids of high-PV tongues related to anticyclonic wave breaking and evaluate the spatiotemporal distributions of RWB events on a 5-degree grid.

TSDs, landfall, TC-induced rainfall, and heavy rainfall

The TC position data is transformed into an area-averaged TS frequency at 4° × 4° grid points. The TSDs are then calculated as the averaged TS occurrence divided by 4 as the TS position data is reported every 6 h.

The LTCs are determined when the TC first comes within 100 km of a coastline, and we match the date of landfall with its corresponding PC indices. Note that we only count the first landfall if a TC experiences multiple landfalls. TC-induced precipitation is calculated by considering the grid points within 500 km of the storm center[49,50]. The precipitation is regarded as zero for those regions without TC-induced precipitation. A heavy rainfall event is defined when the daily mean precipitation rate is >100 mm/day[51], and the rainfall rate is regarded as zero for those regions with the absence of heavy rainfall. Note that the raw precipitation anomalous data is used for TC-induced precipitation and heavy precipitation without band-pass filtering.

Significance test

To test the significance of precipitation anomalies associated with the leading modes (Fig. 4a–c), we apply the *t*-test to test whether the anomalies are different from zero. For the TC-induced precipitation (Fig. 4d–f) and TC landfall rate (Table 1), we use the bootstrap method to shuffle the data and then compare its distribution with the reference data to test whether it can reject the null hypothesis.

Model and hindcast experiments

We use one configuration of the Geophysical Fluid Dynamics Laboratory (GFDL) Seamless System for Prediction and EArth system Research (SPEAR) coupled model, with its horizontal resolution of 50 km for the atmosphere and land models and 100 km for the ocean model[40]. The SPEAR model shares many components with the GFDL CM4.0 model[52]. In particular, SPEAR uses an atmospheric and land model identical to AM4.0/LM4.0[53,54] but with a dynamical vegetation model and a lower resolution MOM6 and SIS2 sea ice model[55].

Using the GFDL SPEAR model, 20-year hindcasts are conducted from 2000 to 2019. Hindcasts are performed every 5 days from June to October (a total of 720 cases) and each has ten ensemble members. A simple nudging technique is adopted for the initialization of both the atmosphere (winds, temperature, and specific humidity) and the ocean (sea surface temperature). The reader is referred to Xiang, et al.[41] for additional details about the hindcast experiments.

Mean square skill score (MSSS). In addition to the correlation skill, we also used the Mean Square Skill Score (MSSS) to measure the skill of deterministic forecasts[56].

The MSSS is defined as follows:

$$MSSS = 1 - \frac{MSE}{MSE_C} \tag{1}$$

where MSE is the mean squared error of the forecast, and MSE_C is the mean squared error of a climatological reference forecast. The mean squared error of the forecasts is:

$$MSE = \frac{1}{n}\sum_{i=1}^{n}(f_i - x_i)^2 \tag{2}$$

where x and f denote time series of observations and forecasts. i and n are the event number and total events.

The MSE for a climatological reference forecast is given by:

$$MSE_C = \frac{1}{n}\sum_{i=1}^{n}(x_i - \overline{x})^2 \tag{3}$$

where $\overline{x}$ is the mean of all cases from observations.

DATA AVAILABILITY

Data related to this study can be downloaded from: ERA-5, https://cds.climate.copernicus.eu/#!/search?text=ERA5&type=dataset, NOAA OLR, https://www.esrl.noaa.gov/psd/data/gridded/data.interp_OLR.html; MSWEP precipitation data, http://www.gloh2o.org/mswep/; TC from National Hurricane Center, https://www.nhc.noaa.gov/data/hurdat/hurdat2-1851-2020-052921.txt; Restrictions apply to the availability of certain SPEAR experiment data, which are under U.S. government regulation. A subset of SPEAR data has been made available via the North American Multi-Model Ensemble Project (https://www.cpc.ncep.noaa.gov/products/NMME/).

CODE AVAILABILITY

All computer codes used to generate results in this paper are available from the corresponding author upon reasonable request.

Received: 7 December 2021; Accepted: 11 July 2022;
Published online: 10 August 2022

REFERENCES

1. Nielsen-Gammon, J., K. A. Reed, S. Elipot, M. Patterson. Research challenge on climate at the coasts. *Tech. Rep.* https://doi.org/10.5065/0g4s-5w68 (2021).
2. Klotzbach, P. J., Bowen, S. G., Pielke, R. & Bell, M. Continental U.S. hurricane landfall frequency and associated damage: observations and future risks. *Bull. Am. Meteorol. Soc.* **99**, 1359–1376 (2018).
3. Smith, A. B. & Matthews, J. L. Quantifying uncertainty and variable sensitivity within the US billion-dollar weather and climate disaster cost estimates. *Nat. Hazards* **77**, 1829–1851 (2015).
4. Willoughby, H. E., Rappaport, E. N. & Marks, F. D. Hurricane forecasting: the state of the art. *Nat. Hazards Rev.* **8**, 45–49 (2007).
5. DeMaria, M., Sampson, C. R., Knaff, J. A. & Musgrave, K. D. Is tropical cyclone intensity guidance improving? *Bull. Am. Meteorol. Soc.* **95**, 387–398 (2014).
6. Chen, J.-H. et al. Advancements in hurricane prediction with NOAA's next-generation forecast system. *Geophys. Res. Lett.* **46**, 4495–4501 (2019).
7. Leroux, M.-D. et al. Recent advances in research and forecasting of tropical cyclone track, intensity, and structure at landfall. *Trop. Cyclone Res. Rev.* **7**, 85–105 (2018).
8. Vecchi, G. A. et al. On the seasonal forecasting of tegional tropical cyclone activity. *J. Clim.* **27**, 7994–8016 (2014).
9. Chen, J.-H. & Lin, S.-J. Seasonal predictions of tropical cyclones using a 25-km-resolution general circulation model. *J. Clim.* **26**, 380–398 (2013).
10. Murakami, H. et al. Seasonal forecasts of major hurricanes and landfalling tropical cyclones using a high-resolution GFDL coupled climate model. *J. Clim.* **29**, 7977–7989 (2016).
11. Lee, C.-Y., Camargo, S. J., Vitart, F., Sobel, A. H. & Tippett, M. K. Subseasonal tropical cyclone genesis prediction and MJO in the S2S dataset. *Weather Forecast* **33**, 967–988 (2018).
12. Lee, C.-Y. et al. Subseasonal predictions of tropical cyclone occurrence and ACE in the S2S dataset. *Weather Forecast.* **35**, 921–938 (2020).
13. Jiang, X. et al. Intraseasonal tropical cyclogenesis prediction in a global coupled model system. *J. Clim.* **31**, 6209–6227 (2018).
14. Li, W. et al. Subseasonal variability of Rossby wave breaking and impacts on tropical cyclones during the North Atlantic warm season. *J. Clim.* **31**, 9679–9695 (2018).
15. Li, W., Wang, Z. & Peng, M. S. Evaluating tropical cyclone forecasts from the NCEP Global Ensemble Forecasting System (GEFS) reforecast version 2. *Weather Forecast* **31**, 895–916 (2016).
16. Landsea, C. W., Pielke, R. A., Mestas-Nuñez, A. M. & Knaff, J. A. Atlantic basin hurricanes: indices of climatic changes. *Clim. Change* **42**, 89–129 (1999).
17. Vecchi, G. A. et al. Statistical? Dynamical predictions of seasonal north atlantic hurricane activity. *Mon. Weather Rev.* **139**, 1070–1082 (2011).
18. Camargo, S. J., Emanuel, K. A. & Sobel, A. H. Use of a genesis potential index to diagnose ENSO effects on tropical cyclone genesis. *J. Clim.* **20**, 4819–4834 (2007).
19. Zhang, R. & Delworth, T. L. Impact of Atlantic multidecadal oscillations on India/Sahel rainfall and Atlantic hurricanes. *Geophys. Res. Lett.* https://doi.org/10.1029/2006GL026267 (2006).
20. Pinto, J. G., Zacharias, S., Fink, A. H., Leckebusch, G. C. & Ulbrich, U. Factors contributing to the development of extreme North Atlantic cyclones and their relationship with the NAO. *Clim. Dyn.* **32**, 711–737 (2009).
21. Elsner, J. B. Tracking hurricanes. *Bull. Am. Meteorol. Soc.* **84**, 353–356 (2003).
22. Villarini, G., Vecchi, G. A. & Smith, J. A. U.S. landfalling and North Atlantic hurricanes: statistical modeling of their frequencies and ratios. *Mon. Weather Rev.* **140**, 44–65 (2012).
23. Murakami, H., Villarini, G., Vecchi, G. A., Zhang, W. & Gudgel, R. Statistical–dynamical seasonal forecast of North Atlantic and U.S. landfalling tropical cyclones using the high-resolution GFDL FLOR coupled model. *Mon. Weather Rev.* **144**, 2101–2123 (2016).
24. Zhang, W., Villarini, G., Vecchi, G. A. & Murakami, H. Impacts of the Pacific meridional mode on landfalling North Atlantic tropical cyclones. *Clim. Dyn.* **50**, 991–1006 (2018).
25. Madden, R. A. & Julian, P. R. Detection of a 40–50 day oscillation in the zonal wind in the tropical pacific. *J. Atmos. Sci.* **28**, 702–708 (1971).
26. Madden, R. A. & Julian, P. R. Description of global-scale circulation cells in the tropics with a 40–50 day period. *J. Atmos. Sci.* **29**, 1109–1123 (1972).
27. Barrett, B. S. & Leslie, L. M. Links between tropical cyclone activity and madden? Julian oscillation phase in the North Atlantic and Northeast Pacific Basins. *Mon. Weather Rev.* **137**, 727–744 (2009).
28. Kossin, J. P., Camargo, S. J. & Sitkowski, M. Climate modulation of North Atlantic hurricane tracks. *J. Clim.* **23**, 3057–3076 (2010).
29. Maloney, E. D. & Hartmann, D. L. Modulation of Hurricane activity in the gulf of mexico by the Madden–Julian oscillation. *Science* **287**, 2002–2004 (2000).
30. Klotzbach, P. J. On the madden?Julian oscillation?Atlantic hurricane relationship. *J. Clim.* **23**, 282–293 (2010).
31. Gao, K. et al. Impact of intraseasonal oscillations on the tropical cyclone activity over the Gulf of Mexico and Western Caribbean sea in GFDL HiRAM. *J. Geophys. Res. Atmos.* **122**, 13125–13137 (2017).
32. Wang, B. & Xie, X. A model for the boreal summer intraseasonal oscillation. *J. Geophys. Res. Atmos.* **54**, 72–86 (1997).
33. Yasunari, T. A quasi-stationary appearance of 30 to 40 day period in the cloudiness fluctuations during the summer monsoon over India. *J. Meteorol. Soc. Jpn. Ser. II* **58**, 225–229 (1980).
34. Camargo, S. J., Wheeler, M. C. & Sobel, A. H. Diagnosis of the MJO modulation of tropical cyclogenesis using an Empirical index. *J. Atmos. Sci.* **66**, 3061–3074 (2009).
35. Wang, B. & Moon, J.-Y. An anomalous genesis potential index for MJO modulation of tropical cyclones. *J. Clim.* **30**, 4021–4035 (2017).

36. Moon, J.-Y., Wang, B., Lee, S.-S. & Ha, K.-J. An intraseasonal genesis potential index for tropical cyclones during Northern hemisphere summer. *J. Clim.* **31**, 9055–9071 (2018).
37. Li, L., Li, W. & Kushnir, Y. Varageriation of the North Atlantic subtropical high western ridge and its implication to Southeastern US summer precipitation. *Clim. Dyn.* **39**, 1401–1412 (2012).
38. Zhang, G. & Wang, Z. North Atlantic Rossby wave breaking during the hurricane season: association with tropical and extratropical variability. *J. Clim.* **32**, 3777–3801 (2019).
39. Helfand, H. M. & Schubert, S. D. Climatology of the simulated great plains low-level jet and its contribution to the continental moisture budget of the United States. *J. Clim.* **8**, 784–806 (1995).
40. Delworth, T. L. et al. SPEAR: The next generation GFDL modeling system for seasonal to multidecadal prediction and projection. *J. Adv. Model Earth Syst.* **12**, e2019MS001895 (2020).
41. Xiang, B. et al. S2S Prediction in GFDL SPEAR: MJO Diversity and Teleconnections. *Bull. Am. Meteorol. Soc.* https://doi.org/10.1175/BAMS-D-21-0124.1 (2021).
42. Harris, L. et al. GFDL SHiELD: A unified system for weather-to-seasonal prediction. *J. Adv. Model Earth Syst.* **12**, e2020MS002223 (2020).
43. Liebmann, B. & Smith, C. A. Description of a complete (interpolated) outgoing longwave radiation dataset. *Bull. Am. Meteorol. Soc.* **77**, 1275–1277 (1996).
44. Beck, H., Yang, L., Pan, M., Wood, E. F. & William, L. *MSWEP V2 Global 3-Hourly 0.1° Precipitation: Methodology and Quantitative Appraisal* (American Geophysical Union, 2017).
45. Landsea, C. W. & Franklin, J. L. Atlantic hurricane database uncertainty and presentation of a new database format. *Mon. Weather Rev.* **141**, 3576–3592 (2013).
46. Abatzoglou, J. T. & Magnusdottir, G. Planetary wave breaking and nonlinear reflection: seasonal cycle and interannual variability. *J. Clim.* **19**, 6139–6152 (2006).
47. Strong, C. & Magnusdottir, G. Tropospheric Rossby wave breaking and the NAO/NAM. *J. Atmos. Sci.* **65**, 2861–2876 (2008).
48. Zhang, G., Wang, Z., Peng, M. S. & Magnusdottir, G. Characteristics and impacts of extratropical Rossby wave breaking during the Atlantic hurricane season. *J. Clim.* **30**, 2363–2379 (2017).
49. Zhang, W. et al. Tropical cyclone precipitation in the HighResMIP atmosphere-only experiments of the PRIMAVERA Project. *Clim. Dyn.* **57**, 253–273 (2021).
50. Dare, R. A., Davidson, N. E. & McBride, J. L. Tropical cyclone contribution to rainfall over Australia. *Mon. Weather Rev.* **140**, 3606–3619 (2012).
51. Kim, J.-H., Ho, C.-H., Lee, M.-H., Jeong, J.-H. & Chen, D. Large increase in heavy rainfall associated with tropical cyclone landfalls in Korea after the late 1970s. *Geophys. Res. Lett.* https://doi.org/10.1029/2006GL027430 (2006).
52. Held, I. M. et al. Structure and performance of GFDL's CM4.0 climate model. *J. Adv. Model Earth Syst.* **11**, 3691–3727 (2019).
53. Zhao, M. et al. The GFDL global atmosphere and land model AM4.0/LM4.0: 1. Simulation characteristics with prescribed SSTs. *J. Adv. Model Earth Syst.* **10**, 691–734 (2018).
54. Zhao, M. et al. The GFDL global atmosphere and land model AM4.0/LM4.0: 2. Model description, sensitivity studies, and tuning strategies. *J. Adv. Model Earth Syst.* **10**, 735–769 (2018).
55. Adcroft, A. et al. The GFDL global ocean and sea ice model OM4.0: model description and simulation features. *J. Adv. Model Earth Syst.* **11**, 3167–3211 (2019).
56. Murphy, A. H. Skill scores based on the mean square error and their relationships to the correlation coefficient. *Mon. Weather Rev.* **116**, 2417–2424 (1988).

ACKNOWLEDGEMENTS

We thank the review comments from Drs. Hiroyuki Murakami, Nathaniel C. Johnson and Zhuo Wang, and also the technical support from Dr. Wenhao Dong. B.W. is supported by the NSF climate dynamics program under award number 2025057.

AUTHOR CONTRIBUTIONS

B.X. conceived of the research, performed model runs, analyzed the model results, and generated figures. W.Z. output the TC precipitation data and contributed to analyze the TC density and landfall frequency. G.Z. provided the Rossby wave breaking data. B.X. wrote the paper with input from all coauthors.

COMPETING INTERESTS

The authors declare no competing interests.

ADDITIONAL INFORMATION

Supplementary information The online version contains supplementary material available at https://doi.org/10.1038/s41612-022-00289-9.

Correspondence and requests for materials should be addressed to Baoqiang Xiang.

Reprints and permission information is available at http://www.nature.com/reprints

Publisher's note Springer Nature remains neutral with regard to jurisdictional claims in published maps and institutional affiliations.